JACS
JOURNAL OF THE AMERICAN CHEMICAL SOCIETY
Article
Cite This: J. Am. Chem. Soc. XXXX, XXX, XXX−XXX
pubs.acs.org/JACS

A Strategy for Increasing the Efficiency of the Oxygen Reduction Reaction in Mn-Doped Cobalt Ferrites

Yin Xiong,[†,#] Yao Yang,[†,#] Xinran Feng,[†,‡] Francis J. DiSalvo,[†] and Héctor D. Abruña*[,†]

[†]Department of Chemistry and Chemical Biology, Cornell University, Ithaca, New York 14850, United States
[‡]Cornell High Energy Synchrotron Source (CHESS), Cornell University, Ithaca, New York 14850, United States

Supporting Information

ABSTRACT: Alkaline fuel cells have drawn increasing attention as next-generation energy-conversion devices for electrical vehicles, since high pH enables the use of non-precious-metal catalysts. Herein, we report on a family of rationally designed Mn-doped cobalt ferrite (MCF) spinel nanocrystals, with an optimal composition $Mn_{0.8}(CoFe_2)_{0.73}O_4$ (MCF-0.8), that are effective electrocatalysts for the oxygen reduction reaction. MCF-0.8 exhibits a half-wave potential ($E_{1/2}$) of 0.89 V vs RHE in 1 M NaOH, only 0.02 V less than that of commercial Pt/C under identical testing conditions and, to the best of our knowledge, one of the highest recorded values in the literature. Moreover, MCF-0.8 exhibits remarkable durability ($\Delta E_{1/2}$ = 0.014 V) after 10 000 electrochemical cycles. *In situ* X-ray absorption spectroscopy (XAS) reveals that the superior performance of the trimetallic MCF-0.8 originates from the synergistic catalytic effect of Mn and Co, while Fe helps preserve the spinel structure during cycling. We employed *in situ* XAS to track the evolution of the oxidation states and the metal−oxygen distances not only under constant applied potentials (steady state) but also during dynamic cyclic voltammetry (CV) (nonsteady state). The periodic conversion between Mn(III, IV)/Co(III) and Mn(II, III)/Co(II) as well as the essentially constant oxidation state of Fe during the CV suggests collaboration efforts among Mn, Co, and Fe. Mn and Co serve as the synergistic coactive sites to catalyze the oxygen reduction, apparently resulting in the observed high activity, while Fe works to maintain the integrity of the spinel structure, likely contributing to the remarkable durability of the catalyst. These findings provide a mechanistic understanding of the electrocatalytic processes of trimetallic oxides under real-time fuel cell operating conditions. This approach provides a new strategy to design high-performance non-precious-metal electrocatalysts for alkaline fuel cells.

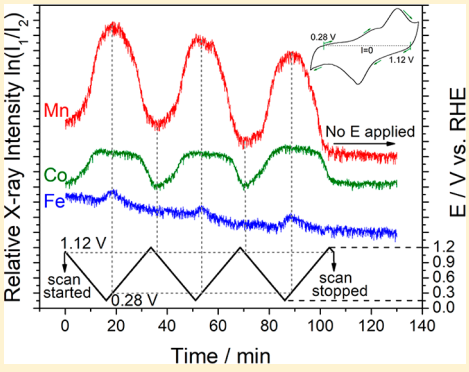

INTRODUCTION

The increasing need for clean, renewable energy continuously stimulates the development of fuel cells, which can exhibit energy conversion efficiency about 3 times higher than that of the internal combustion engine. However, the sluggish kinetics of the oxygen reduction reaction (ORR) at the cathode remains as one of the key challenges.[1,2] To date, state-of-the-art Pt- and Pd-based electrocatalysts are recognized as the most efficient commercial candidates for the ORR in acidic media, but their high cost and scarcity still hinder the widespread large-scale application of proton exchange membrane fuel cells.[3−8] Alternatively, alkaline polymer electrolyte fuel cells (APEFCs) have attracted tremendous attention since they enable the use of nonprecious and earth-abundant materials as electrocatalysts, but they are only resistant to corrosion in alkaline media.[9−13] To lower the ORR overpotential in alkaline media, considerable effort has been devoted to investigating and designing various non-precious-metal catalysts, such as nitrogen-doped carbon,[14,15] transition metal oxides,[16−23] and metal oxynitrides/carbides.[24,25] Recently, the Zhuang group, together with our effort, has reported on an adenosine-derived Fe/N/C catalyst with atomic Fe−N_4 catalytic sites. This material, under the appropriate conditions, achieved a volume-specific activity comparable to commercial Pt/C in rotating-disk electrode experiments and yielded a high peak power density above 450 mW/cm^2 in an APEFC.[15] Dai et al. substituted Co in Co_3O_4 with Mn to form covalent hybrid spinel oxides, $MnCo_2O_4$ loaded on N-doped reduced graphene oxide. This material dramatically enhanced the ORR kinetics, which, they claimed, was due to a covalent coupling effect between spinel oxide nanoparticles and the graphene support.[16,17] Recently, we have reported on a synergistic Mn−Co spinel catalyst with a significantly enhanced ORR activity when compared to the monoxide counterparts.[21] Li et al. utilized a high-pressure pyrolysis process to encapsulate hollow spheres of iron carbide nanoparticles in graphitic layers. The synthesized material exhibited promising ORR activity and stability in both acidic and alkaline media.[25]

Among all of those catalysts, spinel metal oxides represent one of the most promising candidates, due to their high activity, long durability, and low cost. Particularly, spinel metal oxides containing Mn cations have demonstrated to be auspicious ORR electrocatalysts.[16−23] The electrocatalytic activity of

Received: December 23, 2018
Published: February 21, 2019

DOI: 10.1021/jacs.8b13296
J. Am. Chem. Soc. XXXX, XXX, XXX−XXX

Mn-containing spinel oxides is highly dependent on the nominal content of Mn and structural variations. Several reports have found that the ORR performance could be tuned by progressively substituting Mn in $Mn_xM_{3-x}O_4$ (M = Co, Fe, or Cu) spinel oxides.[26−28] In addition, $Co_xFe_{3-x}O_4$, with a cubic spinel structure, has also achieved excellent electrocatalytic activity toward the ORR.[29,30] Despite the substantial progress that has been achieved in the design of more active spinel oxide catalysts, a detailed understanding of the mechanism of oxygen-reduction catalysis using metal oxides remains elusive. Catalysts, normally characterized *ex situ*, may not maintain the same catalytic properties as those under real-time electrochemical conditions, which calls for *in situ* spectroscopy techniques to unveil/identify the true electrocatalytic sites for the ORR.[21]

Herein, we have synthesized a series of manganese cobalt ferrite nanoparticles with the spinel structure of $Mn_x(CoFe_2)_yO_4$ (x ranges from 0 to 1.2, described as MCF-x below). The materials with an optimized composition (MCF-0.8 when x = 0.8) exhibits excellent electrocatalytic performance and remarkable durability after 10 000 CV cycles. A variety of characterization tools, including powder XRD (X-ray diffraction), STEM (scanning transmission electron microscopy) imaging, electron energy loss spectroscopy (EELS) elemental mapping, and energy dispersive spectroscopy (EDX) analysis have been systematically utilized to examine the crystal structures, morphology, and elemental distribution at the atomic scale. Furthermore, *in situ* X-ray absorption spectroscopy (XAS) studies have been carried out to track the changes in the local electronic structures under both steady-state and dynamic non-steady-state conditions. These studies strongly suggest that Mn and Co serve as synergistic electrocatalytic sites, while Fe acts as a structurally stabilizing element that contributes to the long-term durability of the MCF catalysts.

EXPERIMENTAL SECTION

Materials. Iron acetate ($Fe(OAc)_2$), cobalt acetate tetrahydrate ($Co(OAc)_2{\cdot}4H_2O$), manganese acetate tetrahydrate ($Mn(OAc)_2{\cdot}4H_2O$), sodium hydroxide (AR), ammonium hydroxide (25 wt %), nitric acid (HNO_3, 70 wt %), and Nafion (5 wt %) were purchased from Sigma-Aldrich. Carbon-supported Pt/C (20 wt %) nanoparticles (NPs) were supplied by Johnson Matthey. Carbon nanotubes were purchased from Carbon Nanotube Plus. All chemicals were used as received without further purification, except carbon nanotubes, which were treated by soaking in nitric acid overnight and washing for 11 times with deionized water.

Synthesis. MCF nanoparticles, including $CoFe_2O_4$ (MCF-0), $Mn_{0.3}(CoFe_2)_{0.9}O_4$ (MCF-0.3), $Mn_{0.6}(CoFe_2)_{0.8}O_4$(MCF-0.6), $Mn_{0.8}(CoFe_2)_{0.73}O_4$ (MCF-0.8), $Mn_1(CoFe_2)_{0.66}O_4$ (MCF-1), and $Mn_{1.2}(CoFe_2)_{0.6}O_4$ (MCF-1.2) were prepared by a facile hydrothermal method. In a typical synthesis, $Fe(OAc)_2$ (0.25 mmol, 44 mg) and $Co(OAc)_2{\cdot}4H_2O$ (0.125 mmol, 31 mg) were suspended in 20 mL of deionized water, followed by sonicating and stirring for 15 min, respectively. Then, 0.5 mL of $NH_3{\cdot}H_2O$ was added dropwise into the solution under magnetic stirring for another 15 min. A stoichiometric amount of $Mn(OAc)_2{\cdot}4H_2O$ was dissolved in 10 mL of deionized water, ultrasonicated for 10 min, and dropped into the Fe/Co precursor solution. The mixture suspension was maintained at 60 °C in an oil bath for 20 h with constant stirring and was subsequently transferred to a Teflon autoclave, at 130 °C for 3 h. The resulting product was isolated by centrifuging and washed with acetone and 2-propanol three times, respectively. The as-synthesized nanoparticles were dried in an oven at 60 °C overnight and mixed with carbon nanotubes to achieve a 40% mass loading of the metal oxides. The mixture was homogenized by ball milling for 20 min. Finally, the carbon-supported nanoparticles were annealed under Ar at 500 °C for 2 h.

Structural Characterization. The crystal structure of all the synthesized NPs was confirmed by powder XRD using a Rigaku Ultima IV diffractometer. Diffraction patterns were collected at a scan rate of 2° min^{-1} at 0.02° steps from 20° to 80°. STEM images and EELS maps were acquired on a fifth-order aberration-corrected STEM (Cornell Nion UltraSTEM) operated at 100 keV with a beam convergence semiangle of 30 mrad. Sub-angström spatial resolution is achievable under such operating conditions. STEM images were processed using Richard-Lucy deconvolution (3 iterations) (Figure S1). EELS spectral images were acquired with a 0.25 eV/channel energy dispersion in a Gatan spectrometer with a size of 100 × 100 pixels and an acquisition time of 20 ms/pixel. The Mn, Co, and Fe elemental maps were extracted using their sharp L_3 edges from EELS spectral images (Figure S2) and processed using principal component analysis (3 components) and the linear combination of power law to subtract the background in ImageJ software. The crystal models were generated using Crystal Maker software.

Electrochemical Characterization. Electrochemical measurements were performed in 1 M NaOH on a Solartron potentiostat. In all electrochemical measurements, 5 mg of the prepared catalyst was mixed with 2 mL of a 0.05 wt % Nafion/ethanol solution and subsequently sonicated for approximately 30 min. A 20 μL amount of the resulting catalyst ink was loaded onto a 5 mm diameter glassy carbon (GC) electrode, achieving a metal oxide loading of 0.1 mg cm^{-2}, followed by thermal evaporation of the solvent under infrared light. The mass loading of Pt on GC was 25 $\mu g\ cm^{-2}$, a common value, for comparison in fuel cell tests.[8] A graphite rod was used as the counter electrode, and Ag/AgCl, in a 1 M KCl solution, served as the reference electrode. ORR measurements were carried out with a rotating disk electrode (RDE) in oxygen-saturated 1 M NaOH solution at room temperature (23 °C) (bubbling with O_2 for 15 min before scanning). All cyclic voltammetric profiles were obtained between 0.15 and 1.2 V vs a reversible hydrogen electrode (RHE) at 5 mV/s in Ar-saturated 1 M NaOH. The ORR profiles were obtained at 5 mV/s and 1600 rpm after 50 CV cycles from 0.15 to 1.2 V at 50 mV s^{-1} to remove the surface contamination and activate the catalyst. The background capacitive current measured in Ar-saturated 1 M NaOH solution was subtracted to process and plot the ORR profiles. Durability tests were carried out by continuously cycling the potential from 0.6 to 1.0 V at 100 mV/s for 10 000 cycles. The ORR profiles after 10 000 cycles were measured in a fresh 1 M NaOH solution.

***In Situ* X-ray Absorption Measurements.** Mn, Co, and Fe K-edge X-ray absorption near-edge structure (XANES) spectra were acquired at the F-3 beamline of the Cornell High Energy Synchrotron Source (CHESS) from 150 eV below the metal edge out to 550 eV above the edge using nitrogen-filled ion chambers. XANES and EXAFS (extended X-ray absorption fine structure) spectra were calibrated using metal foils and analyzed using the ATHENA software package.[31] Fourier-transformed EXAFS spectra were plotted by applying a Hanning window from 3 to 10 $Å^{-1}$ with k^2-weighting and no phase correction. *In situ* non-steady-state results were obtained by taking transmission measurements for two seconds at the chosen energy. A shutter was used to minimized potential beam damage by blocking the X-ray beam for one second in between data acquisition. Briefly, MCF-0.8 (40 wt %) was dispersed in a Nafion/ethanol (0.05 wt %) solution. Carbon paper (190 μm thick, Fuel Cell Store, AvCarb MGL190) was cut into 1 × 5 cm^2 pieces and used as the catalyst support. The catalyst/ionomer mixture was sprayed on one end of the carbon paper (1 × 1 cm^2) with a metal oxide mass loading of 6 mg/cm^2 using an airbrush, and the rest, 1 × 4 cm^2, served as a nonactive conductor with negligible effects on the catalytic current.

As described in our previous cell design[21] (Figure S3), the electrochemical cell includes two pieces of Teflon, which is chemically inert in the strong base conditions of 1 M saturated NaOH. A Teflon U-shaped sealing ring was placed between the two Teflon pieces, whose distance could be adjusted to make the electrolyte thickness less than 200 μm. On top of the electrochemical cell, a Teflon cap with one gas inlet and another gas outlet was used to bubble N_2 gas to

DOI: 10.1021/jacs.8b13296
J. Am. Chem. Soc. XXXX, XXX, XXX−XXX

minimize the influence of trace amounts of O_2 during electrochemical testing. Inside the electrochemical cell, the section of the carbon paper with the catalyst layer was immersed into the electrolyte near the window for X-ray transmission measurements. A carbon rod was used as the counter electrode (CE) and placed near the working electrode (WE). Ag/AgCl (1 M KCl) was used as the reference electrode (RE) and was placed (via a salt bridge) at the bottom of the cell so that the distance between the WE and RE could be minimized. This, in turn, minimized the *IR* drop during electrochemical testing. All three electrodes were connected to a potentiostat (Biologic SP-200) during *in situ* X-ray data acquisition.

RESULTS AND DISCUSSION

A family of MCF was prepared using a facile hydrothermal method followed by a high-temperature treatment. Their crystal structures were examined by powder XRD, as presented in Figure 1. All of the prepared samples, named $CoFe_2O_4$

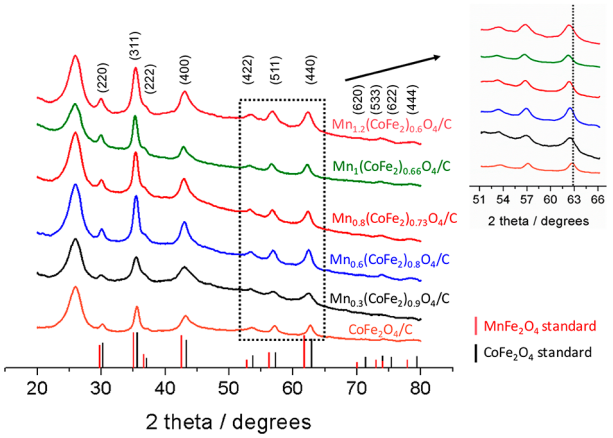

Figure 1. XRD patterns of as-synthesized MCF cubic spinel nanoparticles: $CoFe_2O_4$, $Mn_{0.3}(CoFe_2)_{0.9}O_4$, $Mn_{0.6}(CoFe_2)_{0.8}O_4$, $Mn_{0.8}(CoFe_2)_{0.73}O_4$, $Mn_1(CoFe_2)_{0.66}O_4$, and $Mn_{1.2}(CoFe_2)_{0.6}O_4$. The red and black vertical lines correspond to standard $CoFe_2O_4$ (PDF #01-077-0426) and $MnFe_2O_4$ (PDF #01-073-3820) XRD patterns, respectively; inset represents the enlarged region of the $CoFe_2O_4$ (440) diffraction peak.

(MCF-0), $Mn_{0.3}(CoFe_2)_{0.9}O_4$ (MCF-0.3), $Mn_{0.6}(CoFe_2)_{0.8}O_4$ (MCF-0.6), $Mn_{0.8}(CoFe_2)_{0.73}O_4$ (MCF-0.8), $Mn_1(CoFe_2)_{0.66}O_4$ (MCF-1), and $Mn_{1.2}(CoFe_2)_{0.6}O_4$ (MCF-1.2), possess cubic spinel structures. The broad peak at around 25° in the XRD belongs to carbon, and the remaining diffraction peaks match well with the standard cubic spinel $CoFe_2O_4$ (PDF #01-077-0426, $a = b = c = 8.401$ Å) and $MnFe_2O_4$ (PDF #01-073-3820, $a = b = c = 8.498$ Å). There is a progressive shift to lower 2θ angle at higher Mn contents, corresponding to the gradual substitution of Co and Fe by Mn with larger atomic size. The average domain size of all MCF samples, as estimated from XRD measurements, was found to be around 10−15 nm, which is consistent with STEM images (Figure S4).

The crystal structure of $Mn_{0.8}(CoFe_2)_{0.73}O_4$/C (MCF-0.8) with optimal activity was further examined at the atomic scale using high-angle annular dark-field (HAADF) STEM imaging at 100 keV (Cornell Nion UltraSTEM). Since $CoFe_2O_4$ (a = 8.401 Å) shares a very similar cubic spinel crystal structure to $MnFe_2O_4$ (a = 8.498 Å), the crystal structure of MCF-0.8 from STEM imaging analysis can be built based on the structure of $CoFe_2O_4$ (PDF #01-077-0426). Figure 2A,B present the atomic-scale lattice image of MCF-0.8 and the corresponding

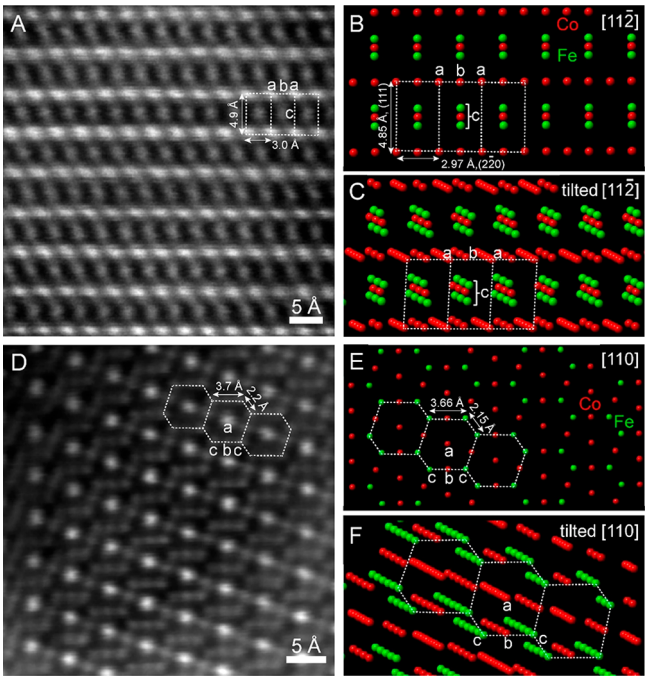

Figure 2. Atomic-scale HAADF-STEM images of MCF-0.8. (A, B) Atomic-scale image and the corresponding crystal model on the [11$\bar{2}$] zone axis. Two lattice d-spacings were measured to be 4.9 and 3.0 Å, which matched well with the theoretical values of (111), 4.85 Å, and (2$\bar{2}$0), 2.97 Å, respectively. Atom columns, **a**, at the corner of the lattice image, exhibit a brighter intensity than atom columns, **b**, on the side, because **a** has higher atom density than that of **b** and **c** in the crystal model. Atom columns, **c**, at the center of the lattice image are elongated in the (111) direction, which are actually composed of three atom columns next to each other. (C) Crystal model on the [11$\bar{2}$] zone axis slightly tilted to reveal the underneath atom columns. (D, E) Another atomic-scale image and the corresponding crystal model on the [110] zone axis. Hexagonal repeating unit cells with two nearby sides of 3.7 and 2.2 Å were observed, which matched the theoretical values of 3.66 and 2.15 Å, respectively, in the crystal model. Atom columns, **a**, at the center of the lattice image, exhibit a brighter intensity than that of columns **b** and **c** on the side, because **a** has a higher atom density than **b** and **c**. Atom columns **b** and **c** show little difference in the image intensity, since they are Co and Fe atoms, with very similar atomic numbers, 27 and 26, respectively. The crystal model was established based on the cubic spinel structure of $CoFe_2O_4$. (F) Crystal model on the [110] zone axis was slightly tilted to reveal the underneath atom columns.

crystal model viewed along the [11$\bar{2}$] zone axis. Two perpendicular d-spacings were measured to be 4.9 and 3.0 Å, well consistent with the theoretical (111), 4.85 Å, and (2$\bar{2}$0), 2.97 Å, lattice planes, respectively. Since the intensity of a HAADF-STEM image is proportional to the atomic number ($I \propto Z^{1.7}$), it is intriguing to observe in Figure 2A that atom columns, **a**, at the corner, exhibit a higher intensity related to that of atom columns, **b**, on the side, even though they are supposed to be the same element, according to the 2D projected crystal model in Figure 2B. This apparent inconsistence can be resolved by deliberately tilting the [11$\bar{2}$] zone axis (Figure 2C) to reveal the atom columns underneath. Despite being the same element, atom columns **a** clearly have a higher atom density than that of atom columns **b**, resulting in a higher image intensity as observed in Figure 2A. It is also observed that atom columns **c** at the center of the lattice image in Figure 2A seem to be elongated in the (111)

DOI: 10.1021/jacs.8b13296
J. Am. Chem. Soc. XXXX, XXX, XXX−XXX

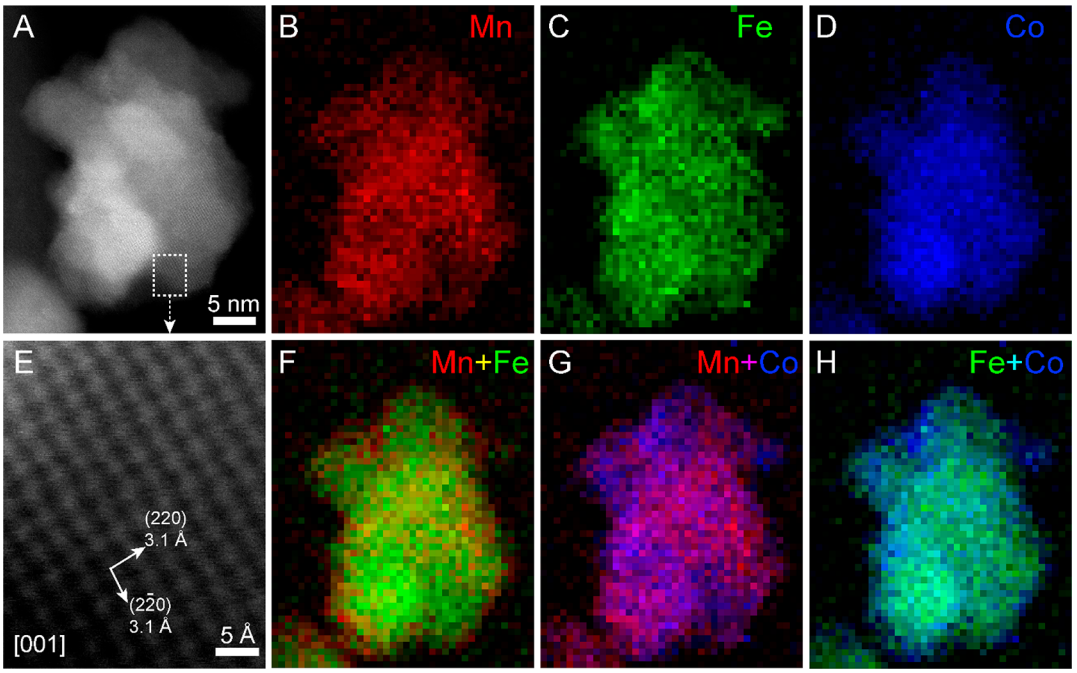

Figure 3. EELS elemental maps of MCF-0.8. (A) HAADF-STEM image of a typical nanoparticle composed of smaller subdomains. The lattice image in the dashed box is magnified in (E) to show (220) and (2$\bar{2}$0) with the same *d*-spacing values of 3.1 Å on the zone axis of [001]. (B–D) EELS elemental maps of Mn (red), Fe (green), and Co (blue), respectively. (F–H) EELS elemental composite maps of Mn vs Fe, Mn vs Co, and Fe vs Co, respectively.

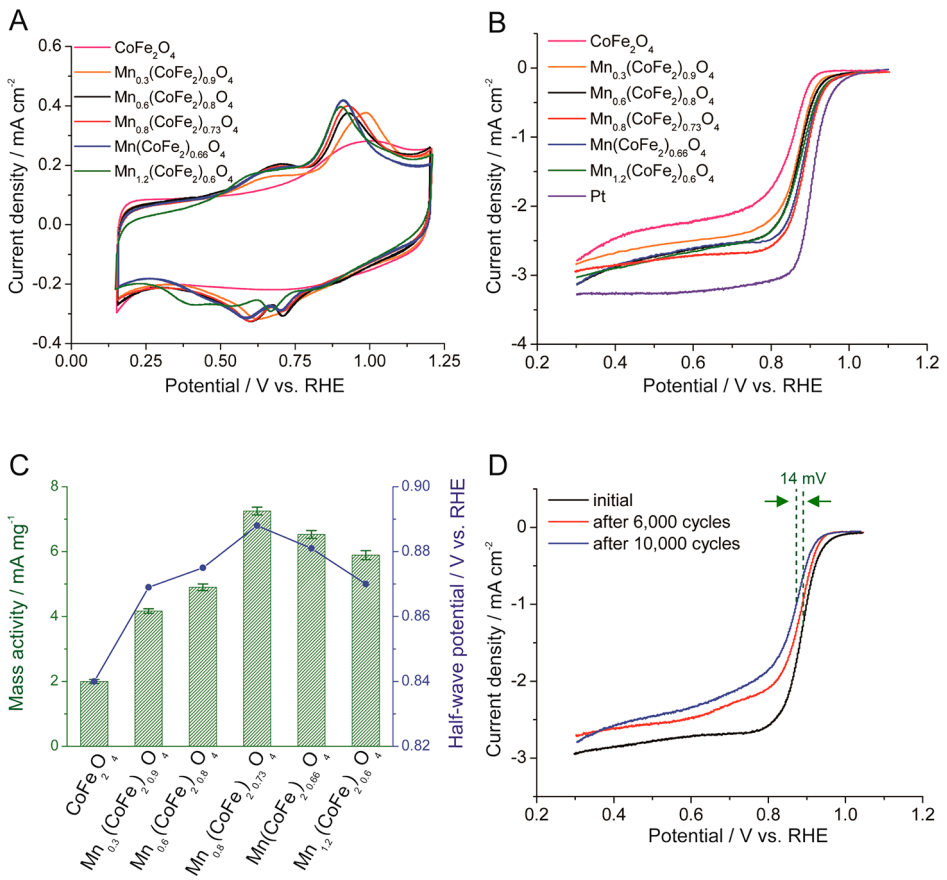

Figure 4. Electrocatalytic properties of as-synthesized MCF nanoparticles. (A) Cyclic voltammetry (CV) profiles of synthesized MCF NPs in Ar-saturated 1 M NaOH solution, scanned at a rate of 5 mV/s at room temperature. (B) ORR polarization curves in O_2-saturated 1 M NaOH at a scan rate of 5 mV/s and rotation at a rate of 1600 rpm. (C) Comparison of mass activity and half-wave potential of different MCFs at 0.9 V vs RHE. (D) Polarization profiles of MCF-0.8 after 10 000 cycles of stability testing.

DOI: 10.1021/jacs.8b13296
J. Am. Chem. Soc. XXXX, XXX, XXX–XXX

direction, which, in fact, corresponds to an assembly of three atom columns next to each other. The distances among the three of them are too short and beyond the spatial resolution of STEM images.

Figure 2D,E exhibit another atomic-scale lattice image of MCF-0.8 and the corresponding crystal model on the more basic [110] zone axis. Hexagonal repeating unit cells are indicated in the dashed boxes with two nearby sides of 3.7 and 2.2 Å with an angle of 125°, which are consistent with the theoretical values of 3.66 and 2.15 Å, respectively, with an angle of 126°. Similar to Figure 2A, atom columns, **a**, at the center of the lattice image in Figure 2D exhibit a higher intensity than that of atom columns, **b** and **c**, on the side. The intensity variations also come from the fact that atom columns **a** have higher atoms density than that of **b** and **c**, as shown in the tilted [110] zone axis (Figure 2F). Noticeably, atom columns **b** and **c** exhibit no significant difference in image intensity, although they could be different element combinations, Co and Fe or Mn and Fe. Given that Mn, Fe, and Co have very similar atomic numbers, the image intensity variations are likely below the noise level threshold of the electron detector. In summary, the aforementioned atomic-scale STEM imaging analysis directly visualized and confirmed the cubic spinel crystal structure of MCF-0.8.

The chemical composition of MCF-0.8 nanoparticles was investigated using EELS elemental mapping. Figure 3A shows a typical MCF-0.8 nanoparticle composed of multiple subdomains. The region in the dashed box is magnified in Figure 3E to show the lattice image, which is on the [001] zone axis with the perpendicular (220) and (2$\bar{2}$0) lattice planes (3.1 Å). Figure 3B−D present the EELS elemental maps of Mn (red), Fe (green), and Co (blue) for the particle in Figure 3A. Figure 3F−H show the composite EELS maps of Mn vs Fe, Mn vs Co, and Fe vs Co. The composite EELS map of Mn vs Fe suggests a homogeneous elemental distribution in which Mn and Fe are intimately mixed on a nearly atomic scale. The composite EELS maps of Mn vs Co and Fe vs Co exhibit a relatively homogeneous elemental distribution with a local enrichment of Co at the edge of the particle. This EELS chemical mapping study combined with the previous analysis of atomic-scale STEM images in Figure 2 unambiguously demonstrate that MCF-0.8 has a cubic spinel crystal structure with a relatively homogeneous elemental distribution of Mn, Co, and Fe.

The cyclic voltammetric profiles of all MCF NPs with different Mn content were obtained in an Ar-saturated 1 M NaOH solution at a scan rate of 5 mV/s from 0.15 to 1.2 V vs RHE, and all are shown in Figure 4A. To identify the redox couples more accurately, the CVs of MCF, together with $CoFe_2O_4$ and $MnFe_2O_4$, were investigated and are presented in Figure S5. There are two redox couples in the 0.15−1.2 V potential window for all Mn-containing oxides. Mn exhibits two oxidative peaks in the positive potential scanning direction, at around 0.68 and 0.91 V, respectively, corresponding to the gradual evolution from Mn(II) to higher valence states (Mn(III, IV)). Conversely, two reductive peaks were observed at 0.72 and 0.6 V repeatedly, indicating the conversion back to Mn(II). Co(III) exhibited a single oxidative peak at around 0.97 V, which overlapped with the more pronounced features from Mn. With increasing Mn and decreasing Co contents, the first peak at higher potential shifts gradually from 0.97 to 0.91 V, which is consistent with the compositional variation. No redox couples from Fe were observed in the CV profiles, as its redox reactions typically occur at more negative potentials.[32,33]

RDE voltammetry was employed to assess the ORR activity of all MCF electrocatalysts. The polarization curves shown in Figure 4B were obtained in 1 M O_2-saturated NaOH solution, at 5 mV/s and 1600 rpm. The half-wave potential ($E_{1/2}$) exhibited a correlation between the electrochemical activity and the Mn content following the order MCF-0 (0.84 V) < MCF-0.3 (0.868 V) < MCF-0.6 (0.875 V) < MCF-1.2 (0.87 V) < MCF-1 (0.88 V) < MCF-0.8 (0.888 V), as shown in Figure 4C (right *y*-axis). With increased Mn content, the kinetics were enhanced at first and then decreased to higher Mn content, with an optimal performance at MCF-0.8, suggesting a "volcano trend". The mass-specific activity (MA) of the MCFs at 0.9 V was calculated by normalizing the kinetic current to the catalyst mass from the Koutecky−Levich equation[34] (Figure 4C, left *y*-axis). MCF-0.8 exhibited the highest MA value of 7.25 mA mg_{oxide}^{-1}, outperforming its counterparts with other Mn contents. To gain further insight into the long-term durability of MCF-0.8, a stability test was carried out in Ar-saturated 1 M NaOH solution for 6000 and 10 000 cycles between 0.6 and 1.0 V, the typical working potential region of APEFCs.[11] There was a progressive negative shift in the polarization curve after 6000 and 10 000 cycles, and the diffusion-limiting current decreased slightly, especially in the high polarization region. The degradation of the electrocatalysts after 10 000 cycles was ascribed to the loss of active material upon extended cycling. This was further confirmed by comparing the CV profiles before and after potential cycles (Figure S6), where the Mn/Co redox peaks gradually faded and broadened as an indication of losing Mn and Co active sites in addition to possible particle aggregation. Despite this minor degradation after durability testing, the MCF-0.8 still exhibited a remarkable ORR electrocatalytic activity, with an $E_{1/2}$ of 0.874 V and $\Delta E_{1/2}$ of only 14 mV after 10000 cycles (Figure 4D).

To further understand the degradation mechanism(s), STEM imaging and EDX spectroscopy were employed to investigate the structural and chemical evolution after cycling. As shown in Figure S7, a STEM image of MCF-0.8 nanoparticles, after electrochemical cycles, clearly indicated particle aggregation/coalescence when compared to the as-synthesized MCF-0.8 in Figure S4. STEM-EDX was used to quantitatively analyze the relative amounts of Co, Fe, and Mn before and after electrochemical cycles. Relative amounts of Co, Fe, and Mn were calculated from the EDX spectra, where the intensity of Fe was normalized to 1 for comparison (Figure S8). It is clear that the Mn loss is nearly 50%, relative to its original content, Co lost around 30%, while the Fe content was stable during the cycling process. The quantitative results were shown in Tables S1−S3. The relative atomic percentages of as-synthesized MCF-0.8 were 29.2, 23.8, and 47.0% for Mn, Co, and Fe, respectively, which is quite consistent with the theoretical ratio of reactants of 27, 24, and 49%. After electrochemical cycling, the relative amounts of Mn and Co dropped from 29.2% to 20.2% and from 23.8% to 18.3%, respectively, while the content of Fe increased from 47.0% to 61.5%.

The superior ORR activity and durability of the trimetallic oxide MCF-0.8 over both $CoFe_2O_4$/C and $MnFe_2O_4$/C suggest that the underlying catalytic mechanism involves multiple metal active sites catalyzing the reduction of oxygen. *In situ* synchrotron-based XAS was employed to investigate the

DOI: 10.1021/jacs.8b13296
J. Am. Chem. Soc. XXXX, XXX, XXX−XXX

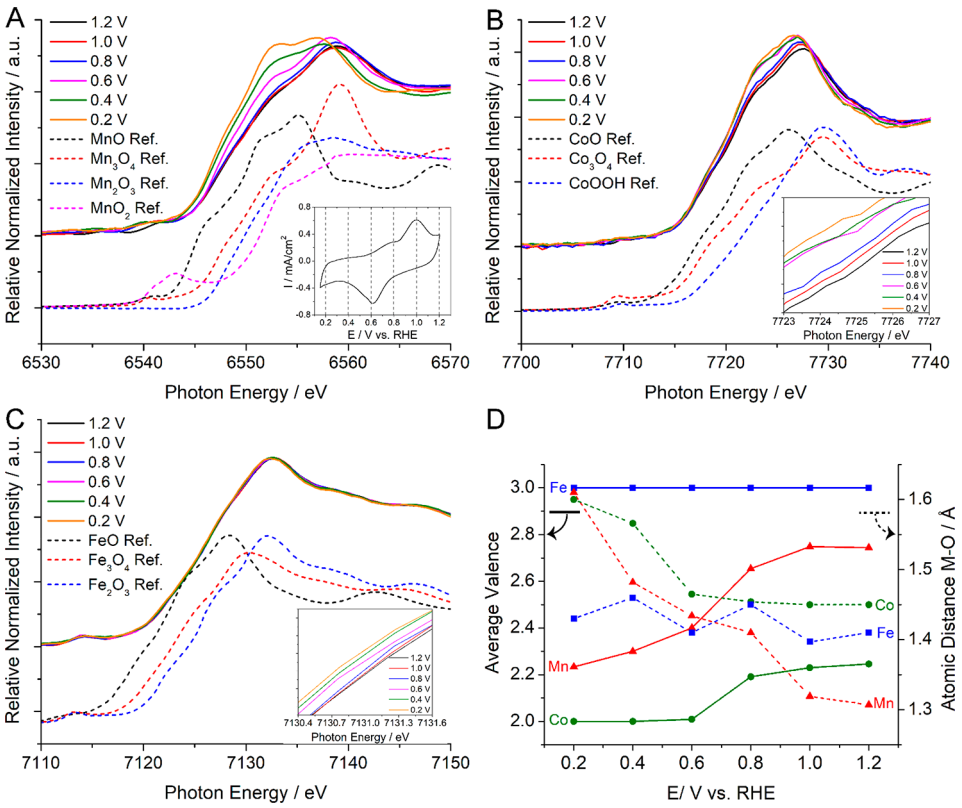

Figure 5. *In situ* XANES spectra of the Mn, Co, and Fe K-edges of MCF-0.8 and the evolution of the average metal valence and metal−oxygen atomic distance at a series of applied potentials. (A) *In situ* XANES spectra at the Mn K-edge of the MCF-0.8 (solid lines) and the reference manganese oxides (dashed lines). Inset shows the selected applied potential from the CV profile at a scan rate of 1 mV/s in the homemade electrochemical cell at which signals were detected. (B) *In situ* XANES spectra at the Co K-edge of the MCF-0.8 (solid lines) and the reference cobalt oxides (dashed lines). Inset shows the gradual shift of the Co K-edge to lower photon energies with changes in intensity. (C) *In situ* XANES spectra at the Fe K-edge of the MCF-0.8 (solid lines) and the reference iron oxides (dashed lines). Inset shows the incremental shift of the Fe K-edge to lower photon energies with a change in intensity. (D) Calculated average metal valence (solid lines, left *y*-axis) as a function of potential based on the linear combination fitting using XANES spectra of reference metal oxides. Measured metal−oxygen (M−O) atomic distance as a function of potential (dashed lines, right *y*-axis) based on the *in situ* EXAFS analysis.

catalytic mechanism of MCF-0.8 under real-time electrochemical conditions. We have designed a customized electrochemical cell for *in situ* XAS measurements in our previous report.[21] The cell consisted of a working electrode of an MCF-0.8 catalyst loaded on porous carbon paper, a Ag/AgCl (1 M KCl) reference electrode, and a carbon rod counter electrode. Details of the cell design can be found in Figure S3. To investigate the structural evolution of the Co−Mn oxide catalysts at steady state, the applied potential was held constant while *in situ* XAS spectra were acquired, after the current had dropped to background levels. According to the CV profile of the catalysts at a scan rate of 1 mV/s in the homemade cell (Figure 5A, inset), constant applied electrochemical potentials (E) of 1.2, 1.0, and 0.8 V vs RHE correspond to the oxidation peak and its two onset potentials, while values of 0.8, 0.6, and 0.4 V vs RHE correspond to the reduction peak and its two onset potentials. An E value of 0.2 V vs RHE was also included to investigate the electrochemical behavior of MCF-0.8 in a strongly reducing environment. Figure 5A exhibits the *in situ* XANES spectra of the Mn K-edge of MCF-0.8 at various applied potentials, suggesting systematic changes in the local electronic structure. Mn XANES spectra were calibrated, based on the characteristic absorption edge of elemental Mn (metal foil) at 6539.0 eV, which corresponds to the excitation of electrons from the Mn 1s orbital. The white line in these Mn spectra, near 6559 eV, originates from an electronic transition from 1s to 4p orbitals, since the 4p are the lowest allowed unoccupied orbitals of 3d transition metals based on the dipole selection rule, $\Delta l = \pm 1$. The shoulder peak at 6553 eV shows a gradual increase in the peak intensity and a small shift to lower energies when the applied potential decreases from 1.2 V to 0.2 V, indicating a lower Mn valence state at more negative potentials. More specifically, this peak at 6553 eV exhibited no significant changes when the potential varies from 1.2 V to 0.8 V and became pronounced when E decreased from 0.8 V to 0.6 V. When the potential was below 0.4 V, it became more prominent and similar to the feature in the MnO(II) reference, qualitatively suggesting a larger contribution from a lower valence Mn.

In order to study the gradual changes in the Mn valence more quantitatively, linear combination fitting (LCF) analysis was performed using pure manganese oxides, MnO(II), Mn_3O_4(II, III), Mn_2O_3(III), and MnO_2(IV), as reference spectra. As shown in Figure S9A, the LCF fits well the experimental Mn XANES spectra and enables the reliable calculation of the relative contributions in of the different Mn oxide references. Figure S9B further demonstrates the evolution of the relative contents of Mn oxide references as E varies from 1.2 V to 0.2 V, as derived from the LCF analysis. When E decreased from 1.2 V to 0.8 V, the relative contents of different metal oxides remained relatively unchanged, corresponding to the little change in the XANES spectra (Figure

DOI: 10.1021/jacs.8b13296
J. Am. Chem. Soc. XXXX, XXX, XXX−XXX

5A). When E continues to decrease from 0.8 V to 0.2 V, the relative contents of MnO_2(IV) and Mn_2O_3(III) quickly dropped from 7% and 10%, respectively, to nearly 0% and the relative contents of Mn_3O_4(II, III) dropped from 60% to 35%. Concomitantly, the relative contents of MnO(II) increased dramatically from 23% to 65%, corresponding to the more dominant features of MnO(II) in XANES spectra of MCF-0.8 at lower potentials. The calculated average valence of Mn decreased substantially and continuously from 2.58 to 2.23 when E decreased from 1.2 V to 0.2 V, as shown in Figure S9B (green line). A lower Mn valence at lower applied potentials would suggest a longer Mn−O chemical bond and weaker binding strength to oxygen, which are clearly confirmed by the corresponding *in situ* EXAFS spectra in Figure S10A. The Mn−O atomic distance increased continuously from 1.31 Å to 1.61 Å when E decreased from 1.2 V to 0.2 V, as shown in Figure S10A (black dashed line). This systematic evolution of the Mn valence and the M−O atomic distance strongly indicates that various Mn species can serve as the active site to catalyze the oxygen reduction reaction.

Co K-edge XANES spectra exhibited similar changes to those of Mn in the MCF-0.8 electrocatalyst (Figure 5B). Co XANES spectra were calibrated based on the characteristic absorption edge of elemental Co (metal foil) at 7709.0 eV. The *in situ* Co XANES spectra and the magnified inset in Figure 5B exhibit a gradual increase in the peak intensity at around 7725 eV and a continuous shift to lower energies when E decreased from 1.2 V to 0.2 V, indicating lower Co valences at lower applied potentials. The absorption edge of Co had the most significant changes when E dropped from 0.8 V to 0.6 V, indicating an abrupt change in its oxidation state and electronic environment. LCF analysis was also employed to quantitatively study the Co valence with CoO(II), Co_3O_4(II, III), and CoOOH(III) as cobalt oxide references (Figure S9C). When E varied from 1.2 V to 0.6 V, the relative contents of CoOOH decreased from 24% to nearly 0%, while that of CoO increased from 76% to nearly 100%, corresponding to the abrupt change in XANES spectra in Figure 5B. The XANES spectra of Co remained essentially unchanged with 100% CoO when the applied E further was decreased from 0.6 V to 0.2 V. In contrast to changes of relative contents of Mn_3O_4, the relative contents of Co_3O_4 were calculated to be consistently zero at various potentials, suggesting a negligible contribution from Co_3O_4. The calculated average valence of Co decreased from 2.246 to 2.0 when E varied from 1.2 V to 0.6 V and stayed at 2.0 from 0.6 V to 0.2 V, as shown in Figure S9D (green line). *In situ* EXAFS of Co further revealed that the Co−O atomic distance gradually became longer, from 1.45 Å to 1.60 Å, when E shifted from 1.2 V to 0.2 V, as shown in Figure S10B (black dashed line). This is consistent with the lower Co valence at lower applied potentials, suggesting a weaker Co binding strength to oxygen. Although the gradual evolution of the average Co valence and Co−O atomic distance at various applied potentials were less pronounced than for Mn, the changes in the valence state of Co and Mn shared a similar pattern, suggesting that Co and Mn could serve as coactive sites to catalyze the reduction of oxygen.

Contrary to Co and Mn, the *in situ* XANES of Fe at the K-edge indicated no significant changes during the entire potential range from 1.2 to 0.2 V (Figure 5C). The magnified inset exhibits a small increase in the peak intensity at around 7131 eV and a slight shift to lower energies. Further LCF analysis of the Fe valence suggests a 100% contribution from Fe_2O_3(III) at 1.2 V (Figure S11). The Fe valence remained unchanged over the entire E range, from 1.2 V to 0.2 V, when considering the small statistical error of the LCF analysis (reduced $\chi^2 < 0.001$). The *in situ* EXAFS spectra around the Fe K-edge in Figure S12 suggest that the Fe−O atomic distance remained relatively stable at 1.43 Å with no more than ±0.05 Å variation when E decreased from 1.2 V to 0.2 V. Given the above analysis of the average Fe valence and the Fe−O interatomic distance, unlike Co and Mn, the local electronic structure of Fe stays relatively unchanged over a wide potential range from 1.2 to 0.2 V, indicating that Fe can serve as a "stabilizing agent" in MCF-0.8 and, at least in part, contribute to the remarkable durability of MCF-0.8 even after 10 000 electrochemical cycles.

Figure 5D serves as a compact summary of the dynamic evolution of average metal valence (solid lines, left y-axis) and metal−oxygen (M−O) interatomic distance (dashed lines, right y-axis) at various applied potentials. The average Mn and Co valences share a similar decreasing trend at lower applied potentials (red and green solid lines), but some differences in the details can be noted. The Mn−O distance continuously and dramatically decreased from 2.581 Å to 2.233 Å, while the Co−O distance decreased from 2.246 Å to 2.000 Å when E varied from 1.2 to 0.6 V and remained at 2.000 Å even when E was below 0.6 V. Considering that the typical working voltages of the membrane electrode assembly (MEA) in alkaline fuel cells are from 0.6 to 1.0 V,[11] the dynamic changes of the valence of Mn and Co suggested that both could serve as active sites and catalyze the reduction of oxygen. The Mn−O atomic distance increased at lower potentials, which is consistent with the decrease of Mn valence at lower potentials, suggesting a weaker binding energy of Mn toward oxygen. Changes of the Co−O interatomic distance followed a similar pattern though with less pronounced changes than for Mn at various potentials (dashed green line). The Co−O interatomic distance continuously increased when E was below 0.6 V, while the Co valence mainly remained at 2.0, indicating that other factors in the electronic structure and local chemical environment may also influence the binding energy of Co toward oxygen. The lack of significant changes in the Fe valence and the Fe−O interatomic distance (solid and dashed blue lines) suggest that Fe could serve as a stabilizing core element to maintain the integrity of the spinel structure and enhance the long-term durability.

We investigated the evolution of the local electronic structures of Mn, Co, and Fe using *in situ* XANES and EXAFS under steady-state, constant applied potential conditions. We then explored the dynamic changes in the valence state of the metal active sites during CV. Such experiments require a nonconventional strategy to enable fast recording of absorption differences, of transmitted X-rays, down to the level of seconds, so as to enable following the relatively fast potential changes during CV. This strategy was first reported in our previous study[21] and employed in this work to enable understanding the synergistic effects of the multiactive sites in MCF-0.8. Instead of acquiring a full XAS spectrum over a long period (20−30 min), the absorbed X-ray intensity variations were recorded within seconds, at a characteristic energy where the largest changes in the intensity of absorption occurred in the above-mentioned steady-state measurements (Figure 5A). The X-ray absorption intensity was calculated as $\ln(I_1/I_2)$ where I_1 and I_2 are the incident and transmitted X-ray beam intensities, respectively. In this particular case, the

DOI: 10.1021/jacs.8b13296
J. Am. Chem. Soc. XXXX, XXX, XXX−XXX

characteristic energy values of Mn, Co, and Fe were determined to be 6553, 7225, and 7131 eV, respectively. A scan rate of 1 mV/s, combined with an X-ray acquisition time of 3 s, indicates that the X-ray signal will be averaged over a 3 mV potential range, closely approximating non-steady-state (dynamic) measurements. From the CV profile at 1 mV/s in the upper inset of Figure 6, we observed that the oxidation

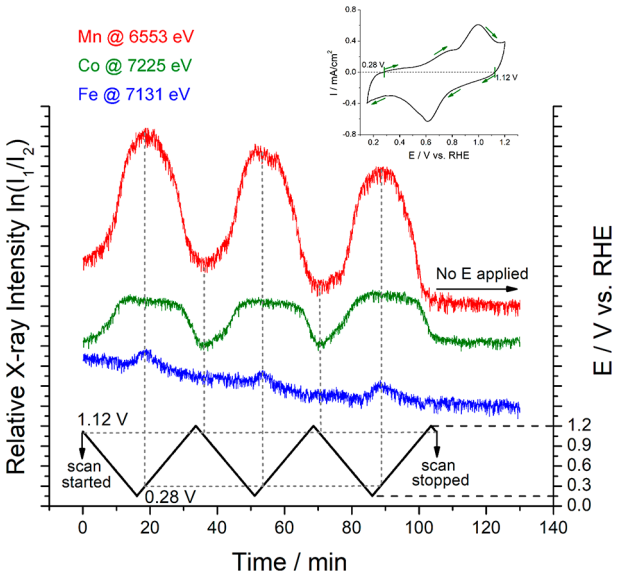

Figure 6. Periodic changes of the relative X-ray intensities ($\ln(I_1/I_2)$) at 6553 eV (Mn K-edge, red lines), 7225 eV (Co K-edge, green lines), and 7131 eV (Fe K-edge, blue lines), respectively, as a function of the cyclic potential sweep at 1 mV/s from 1.2 to 0.15 V vs RHE. Intensity variations at 6553, 7225, and 7131 eV reflect the conversion among Mn(IV), Mn(III), and Mn(II), between Co(III) and Co (II), and between Fe(III) and Fe(II), respectively. Relative X-ray intensity increases, suggesting a conversion of the metal from higher valence to lower valence as the applied potential goes from 1.2 to 0.15 V, and reaches a maximum value at 0.28 V. Concomitantly, the relative X-ray intensity decreased as the applied potential goes from 0.15 to 1.2 V and reaches a maximum value at 1.12 V. The upper inset shows the corresponding CV at 1 mV/s over the potential range of 0.15−1.2 V vs RHE. Oxidation and reduction currents in the CV are divided by two boundary potentials, 0.28 and 1.12 V vs RHE.

currents (positive values) and the reduction currents (negative values) were divided by two boundary potentials, 1.12 and 0.28 V. One would expect that the oxidation/reduction currents will reflect metal active sites being converted into higher/lower valence states and that a periodic change of the metal valence will follow the triangular potential scan (*vide infra*).

Figure 6 reveals the periodic changes in the relative X-ray intensity, $\ln(I_1/I_2)$, as a cyclic potential scan is applied. When the applied potential starts at the upper boundary value, 1.12 V, and is scanned to the lower limit, 0.15 V, the relative X-ray intensity of Mn increases dramatically and keeps increasing to the maximum intensity until the potential passes the lower limit, 0.15 V, and reaches the lower boundary potential, 0.28 V. Higher X-ray intensities, as shown in Figure 5A, indicate higher contents of lower Mn valence since the selected energy is closer to the Mn(II) white line energy. The processes from 1.12 to 0.28 V represent the conversion from Mn(III, IV) to Mn(II, III). Symmetrically, when the potential varies from the lower boundary potential, 0.28 V, to the upper limit, 1.2 V, the X-ray intensity keeps decreasing to the minimum values until the potential first passes the upper limit, 1.2 V, and reaches the upper boundary potential, 1.12 V. The processes from 0.28 to 1.12 V represent the conversion from Mn(II, III) to Mn(III, IV). Mn valences change in a periodic fashion in the subsequent two cyclic potential scans. This is fully consistent with the boundary potentials (0.28, 1.12 V) of oxidation and reduction currents in the CV discussed before, unveiling a real-time glimpse of an intriguing electrocatalytic mechanism of Mn active sites in MCF-0.8.

Compared to the changes of Mn, the relative X-ray intensity of Co at 7225 eV also increases as the potential drops from 1.12 V, but reaches a relatively stable plateau at around 0.6 V, which is consistent with the dramatic changes in the Co XANES spectra from 1.2 to 0.6 V with few, if any, changes below 0.6 V (Figure 5B). During the cyclic potential scan, the periodic behavior of the relative X-ray intensity of Co corresponds to the reversible conversion between Co(III) at high E and Co(II) at lower E. In sharp contrast to the patterns of Mn and Co, the relative X-ray intensity of Fe at 7131 eV remains essentially unchanged during the cyclic potential scan, suggesting no significant changes in the Fe valence. A smaller X-ray intensity variation of Fe evident at very negative potentials at around 0.15−0.28 V may suggest a slight reduction from Fe(III) to Fe(II), which is consistent with the incremental increase in the X-ray intensity of the Fe K-edge XANES (Figure 5C). Such a small conversion from Fe(III) to Fe(II) may not be revealed in the change of Fe valence, considering the statistical error of LCF analysis.

The relative changing X-ray intensities of Mn, Co, and Fe following repeating patterns during three continuous cyclic potential scans suggest a reproducible and stable electrochemical behavior of the three metal active sites under electrochemical operating conditions. To rigorously exclude other factors, such as X-ray-generated photoelectrons, which may result in periodic patterns of X-ray intensity variations, a control experiment was performed by recording the X-ray signal without an applied potential. A stable background in the X-ray intensity indicates that the periodic changes of Mn and Co valences primarily arise from the applied cyclic potential scan. In summary, the periodic patterns of Mn and Co valence changes in MCF-0.8 are in sync with each other, which strongly suggests a synergistic effect existing between Mn and Co for the electrocatalysis toward the reduction of oxygen. Fe, in contrast, maintains a stable electronic structure and serves as a supportive core element, which may contribute to the long-term durability.

CONCLUSIONS

In summary, a new class of MCF nanoparticle electrocatalysts for the ORR has been rationally designed and prepared via hydrothermal reaction and subsequent heat treatment. Their electrochemical activity demonstrates a "volcano trend" correlation with continuously increasing Mn content. The MCF-0.8 had the most active composition, exhibiting an ORR activity with an $E_{1/2}$ of 0.89 V, nearly the same as Pt/C, and a robust durability with a $\Delta E_{1/2}$ of 0.014 V after 10 000 potential cycles. A thorough mechanistic picture emerged from the *in situ* XAS experiment, suggesting that the Mn and Co cations serve as the active sites, with Fe stabilizing the spinel oxide structure. Additionally, the comprehensive STEM-EDX quantitative analysis provided additional evidence of the synergistic effect toward the oxygen reduction reaction and possible explanations for the degradation process. The work

DOI: 10.1021/jacs.8b13296
J. Am. Chem. Soc. XXXX, XXX, XXX−XXX

outlined here sheds light on the strategic design of trimetallic spinel oxides as ORR electrocatalysts in alkaline fuel cells and advances our understanding of the catalytic mechanism using *operando* spectroscopic methods.

■ ASSOCIATED CONTENT

Supporting Information

The Supporting Information is available free of charge on the ACS Publications website at DOI: 10.1021/jacs.8b13296.

Figure S1−S12; Tables S1−S3 (PDF)

■ AUTHOR INFORMATION

Corresponding Author

*hda1@cornell.edu

ORCID

Yao Yang: 0000-0003-0321-3792

Héctor D. Abruña: 0000-0002-3948-356X

Author Contributions

#Y. Xiong and Y. Yang contributed equally to this work.

Notes

The authors declare no competing financial interest.

■ ACKNOWLEDGMENTS

This work was primarily supported by the Center for Alkaline-Based Energy Solutions (CABES) and the Center for Energy Materials at Cornell (emc^2), part of the Energy Frontier Research Center (EFRC) program supported by the U.S. Department of Energy, under grant DE-SC-0019445. Y.Y. made use of TEM facilities at the Cornell Center for Materials Research (CCMR), which are supported through the National Science Foundation Materials Research Science and Engineering Center (NSF MRSEC) program (DMR-1719875). Y.Y. thanks Malcolm (Mick) Thomas at CCMR for the help in Nion UltraSTEM. The *in situ* XRD work is based upon research conducted at the Cornell High Energy Synchrotron Source (CHESS), which is supported by the National Science Foundation under award DMR-1332208. X.F. also acknowledges financial support from CHESS under the same award. We deeply appreciate the invaluable long-term assistance of CHESS staff scientists Rong Huang and Peter Ko.

■ REFERENCES

(1) Debe, M. K. Electrocatalyst Approaches and Challenges for Automotive Fuel Cells. *Nature* **2012**, *486*, 43−51.

(2) Xiong, Y.; Yang, Y.; Joress, H.; Padgett, E.; Gupta, U.; Yarlagadda, V.; Agyeman-Budu, D. N.; Huang, X.; Moylan, T. E.; Zeng, R.; Kongkanand, A.; Escobedo, F. A.; Brock, J. D.; DiSalvo, F. J.; Muller, D. A.; Abruña, H. D. Revealing the Atomic Ordering of Binary Intermetallics Using in Situ Heating Techniques at Multilength Scales. *Proc. Natl. Acad. Sci. U. S. A.* **2019**, *116*, 1974−1983.

(3) Gasteiger, H. A.; Kocha, S. S.; Sompalli, B.; Wagner, F. T. Activity Benchmarks and Requirements for Pt, Pt-alloy, and Non-Pt Oxygen Reduction Catalysts for PEMFCs. *Appl. Catal., B* **2005**, *56*, 9−35.

(4) Shao, M.; Chang, Q.; Dodelet, J.-P.; Chenitz, R. Recent Advances in Electrocatalysts for Oxygen Reduction Reaction. *Chem. Rev.* **2016**, *116*, 3594−3657.

(5) Chung, H. T.; Cullen, D. A.; Higgins, D.; Sneed, B. T.; Holby, E. F.; More, K. L.; Zelenay, P. Direct Atomic-level Insight into the Active Sites of a High-Performance PGM-Free ORR Catalyst. *Science* **2017**, *357*, 479−484.

(6) Stamenkovic, V. R.; Mun, B. S.; Arenz, M.; Mayrhofer, K. J.; Lucas, C. A.; Wang, G.; Ross, P. N.; Markovic, N. M. Trends in Electrocatalysis on Extended and Nanoscale Pt-Bimetallic Alloy Surfaces. *Nat. Mater.* **2007**, *6*, 241−247.

(7) Wang, D.; Xin, H. L.; Hovden, R.; Wang, H.; Yu, Y.; Muller, D. A.; DiSalvo, F. J.; Abruña, H. D. Structurally Ordered Intermetallic Platinum−Cobalt Core−Shell Nanoparticles with Enhanced Activity and Stability as Oxygen Reduction Electrocatalysts. *Nat. Mater.* **2013**, *12*, 81−87.

(8) Xiong, Y.; Yang, Y.; DiSalvo, F. J.; Abruña, H. D. Pt-Decorated Composition-Tunable Pd-Fe@ Pd/C Core-Shell Nanoparticles with Enhanced Electrocatalytic Activity towards the Oxygen Reduction Reaction. *J. Am. Chem. Soc.* **2018**, *140*, 7248−7255.

(9) Xiong, Y.; Xiao, L.; Yang, Y.; DiSalvo, F. J.; Abruña, H. D. High-Loading Intermetallic Pt_3Co/C Core−Shell Nanoparticles as Enhanced Activity Electrocatalysts toward the Oxygen Reduction Reaction (ORR). *Chem. Mater.* **2018**, *30*, 1532−1539.

(10) Lima, F. H. B.; Zhang, J.; Shao, M.; Sasaki, K.; Vukmirovic, M. B.; Ticianelli, E. A.; Adzic, R. R. Catalytic Activity-d-Band Center Correlation for the O_2 Reduction Reaction on Platinum in Alkaline Solutions. *J. Phys. Chem. C* **2007**, *111*, 404−410.

(11) Lu, S.; Pan, J.; Huang, A.; Zhuang, L.; Lu, J. Alkaline Polymer Electrolyte Fuel Cells Completely Free from Noble Metal Catalysts. *Proc. Natl. Acad. Sci. U. S. A.* **2008**, *105*, 20611−20614.

(12) Wang, Y.-J.; Qiao, J.; Baker, R.; Zhang, J. Alkaline Polymer Electrolyte Membranes for Fuel Cell Applications. *Chem. Soc. Rev.* **2013**, *42*, 5768−5787.

(13) Ge, X.; Sumboja, A.; Wuu, D.; An, T.; Li, B.; Thomas Goh, F. W.; Andy Hor, T. S.; Zong, Y.; Liu, Z. Oxygen Reduction in Alkaline Media: from Mechanisms to Recent Advances of Catalysts. *ACS Catal.* **2015**, *5*, 4643−4667.

(14) Jiang, W.-J.; Gu, L.; Li, L.; Zhang, Y.; Zhang, X.; Zhang, L.-J.; Wang, J.-Q.; Hu, J.-S.; Wei, Z.; Wan, L.-J. Understanding the High Activity of Fe−N−C Electrocatalysts in Oxygen Reduction: Fe/Fe_3C Nanoparticles Boost the Activity of Fe−N_x. *J. Am. Chem. Soc.* **2016**, *138*, 3570−3578.

(15) Ren, H.; Wang, Y.; Yang, Y.; Tang, X.; Peng, Y.; Peng, H.; Xiao, L.; Lu, J.; Abruña, H. D.; Zhuang, L. Fe/N/C Nanotubes with Atomic Fe sites: A Highly Active Cathode Catalyst for Alkaline Polymer Electrolyte Fuel Cells. *ACS Catal.* **2017**, *7*, 6485−6492.

(16) Liang, Y.; Li, Y.; Wang, H.; Zhou, J.; Wang, J.; Regier, T.; Dai, H. Co_3O_4 Nanocrystals on Graphene as a Synergistic Catalyst for Oxygen Reduction Reaction. *Nat. Mater.* **2011**, *10*, 780−786.

(17) Liang, Y.; Wang, H.; Zhou, J.; Li, Y.; Wang, J.; Regier, T.; Dai, H. Covalent Hybrid of Spinel Manganese−Cobalt Oxide and Graphene as Advanced Oxygen Reduction Electrocatalysts. *J. Am. Chem. Soc.* **2012**, *134*, 3517−3523.

(18) Cheng, F.; Shen, J.; Peng, B.; Pan, Y.; Tao, Z.; Chen, J. Rapid Room-Temperature Synthesis of Nanocrystalline Spinels as Oxygen Reduction and Evolution Electrocatalysts. *Nat. Chem.* **2011**, *3*, 79−84.

(19) Li, C.; Han, X.; Cheng, F.; Hu, Y.; Chen, C.; Chen, J. Phase and Composition Controllable Synthesis of Cobalt Manganese Spinel Nanoparticles towards Efficient Oxygen Electrocatalysis. *Nat. Commun.* **2015**, *6*, 7345.

(20) Zhao, Q.; Yan, Z.; Chen, C.; Chen, J. Spinels: Controlled Preparation, Oxygen Reduction/Evolution Reaction Application, and Beyond. *Chem. Rev.* **2017**, *117*, 10121−10211.

(21) Yang, Y.; Wang, Y.; Xiong, Y.; Huang, X.; Shen, L.; Huang, R.; Wang, H.; Pastore, J. P.; Yu, S.-H.; Xiao, L.; Brock, J. D.; Zhuang, L.; Abruña, H. D. In Situ X-ray Absorption Spectroscopy of a Synergistic Co−Mn Oxide Catalyst for the Oxygen Reduction Reaction. *J. Am. Chem. Soc.* **2019**, *141*, 1463−1466.

(22) Meng, Y.; Song, W.; Huang, H.; Ren, Z.; Chen, S.-Y.; Suib, S. L. Structure−Property Relationship of Bifunctional MnO_2 Nanostructures: Highly Efficient, Ultra-Stable Electrochemical Water Oxidation and Oxygen Reduction Reaction Catalysts Identified in Alkaline Media. *J. Am. Chem. Soc.* **2014**, *136*, 11452−11464.

(23) Lee, J. W.; Hall, A. S.; Kim, J. D.; Mallouk, T. E. A Facile and Template-Free Hydrothermal Synthesis of Mn_3O_4 Nanorods on Graphene Sheets for Supercapacitor Electrodes with Long Cycle Stability. *Chem. Mater.* **2012**, *24*, 1158−1164.

DOI: 10.1021/jacs.8b13296
J. Am. Chem. Soc. XXXX, XXX, XXX−XXX

(24) Miura, A.; Rosero-Navarro, C.; Masubuchi, Y.; Higuchi, M.; Kikkawa, S.; Tadanaga, K. Nitrogen-Rich Manganese Oxynitrides with Enhanced Catalytic Activity in the Oxygen Reduction Reaction. *Angew. Chem., Int. Ed.* **2016**, *55*, 7963−7967.
(25) Hu, Y.; Jensen, J.; Zhang, W.; Cleemann, L.; Xing, W.; Bjerrum, N.; Li, Q. Hollow Spheres of Iron Carbide Nanoparticles Encased in Graphitic Layers as Oxygen Reduction Catalysts. *Angew. Chem.* **2014**, *126*, 3749−375.
(26) Zhu, H.; Zhang, S.; Huang, Y.-X.; Wu, L.; Sun, S. Monodisperse $M_xFe_{3-x}O_4$ (M = Fe, Cu, Co, Mn) Nanoparticles and Their Electrocatalysis for Oxygen Reduction Reaction. *Nano Lett.* **2013**, *13*, 2947−2951.
(27) Restovic, A.; Ríos, E.; Barbato, S.; Ortiz, J.; Gautier, J. Oxygen Reduction in Alkaline Medium at Thin $Mn_xCo_{3-x}O_4$ ($0 \leq x \leq 1$) Spinel Films Prepared by Spray Pyrolysis. Effect of Oxide Cation Composition on the Reaction Kinetics. *J. Electroanal. Chem.* **2002**, *522*, 141−151.
(28) Ríos, E.; Abarca, S.; Daccarett, P.; Cong, H. N.; Martel, D.; Marco, J.; Gancedo, J.; Gautier, J. Electrocatalysis of Oxygen Reduction on $Cu_xMn_{3-x}O_4$ ($1.0 \leq x \leq 1.4$) Spinel Particles/Polypyrrole Composite Electrodes. *Int. J. Hydrogen Energy* **2008**, *33*, 4945−4954.
(29) Indra, A.; Menezes, P.; Sahraie, N.; Bergmann, A.; Das, C.; Tallarida, M.; Schmeißer, D.; Strasser, P.; Driess, M. Unification of Catalytic Water Oxidation and Oxygen Reduction Reactions: Amorphous Beat Crystalline Cobalt Iron Oxides. *J. Am. Chem. Soc.* **2014**, *136*, 17530−17536.
(30) Wu, G.; Wang, J.; Ding, W.; Nie, Y.; Li, L.; Qi, X.; Chen, S.; Wei, Z. A strategy to Promote the Electrocatalytic Activity of Spinels for Oxygen Reduction by Structure Reversal. *Angew. Chem.* **2016**, *128*, 1362−1366.
(31) Ravel, B.; Newville, M. ATHENA, ARTEMIS, HEPHAESTUS: Data Analysis for X-ray Absorption Spectroscopy Using IFEFFIT. *J. Synchrotron Radiat.* **2005**, *12*, 537.
(32) Castro, P.; Vago, E.; Calvo, E. Surface Electrochemical Transformations on Spinel Iron Oxide Electrodes in Aqueous Solutions. *J. Chem. Soc., Faraday Trans.* **1996**, *92*, 3371.
(33) Zhou, Y.; Xi, S.; Wang, J.; Sun, S.; Wei, C.; Feng, Z.; Du, Y.; Xu, Z. J. Revealing the Dominant Chemistry for Oxygen Reduction Reaction on Small Oxide Nanoparticles. *ACS Catal.* **2018**, *8*, 673−677.
(34) Bard, A. J.; Faulkner, L. R. *Electrochemical Methods: Fundamentals and Applications*; Wiley: New York, 2001; p 341.

DOI: 10.1021/jacs.8b13296
J. Am. Chem. Soc. XXXX, XXX, XXX−XXX